Numerical modelling of forming of a non-crimp 3D orthogonal weave E-glass composite reinforcement

Juan Pazmino [a], Sylvain Mathieu [b], Valter Carvelli [a,*], Philippe Boisse [b], Stepan V. Lomov [c]

[a] Department of Architecture, Built Environment and Construction Engineering, Politecnico di Milano, Piazza Leonardo da Vinci 32, 20133 Milan, Italy
[b] Laboratoire de Mécanique des Contacts et des Solides UMR CNRS 5514, INSA de Lyon, Bâtiment Jacquard, Rue Jean Capelle, 69621 Villeurbanne, France
[c] Department of Materials Engineering, K.U. Leuven, Kasteelpark Arenberg 44, B-3001 Leuven, Belgium

Received 11 November 2014
Received in revised form 24 January 2015
Accepted 14 February 2015
Available online 24 February 2015

1. Introduction

Since the late 1960s, various types of polymer composites reinforced with 3D textiles have been developed to overcome some of the problems that are inherent with conventional laminates, i.e. their low delamination fracture toughness and poor impact damage tolerance [1]. Three-dimensional textile reinforcements include yarns oriented not only in-plane but also in the through-thickness direction, which results in higher out-of-plane strength and stiffness of the final composite component [2]. The versatility of their production processes allows for the usage of different types of yarns and different weave patterns in various parts of the reinforcement, opening a wide design window. In addition, 3D reinforcements offer possibilities of improving the manufacturing quality by minimizing ply slippage and lowering the manufacturing cost by shortening the preform lay-up time [2].

Composite components with complex shapes are generally obtained by liquid moulding (LCM) processes due to their low equipment and tooling costs, low pressure requirements, short cycle times and ability to yield net-shape parts [3]. The first stage of such processes consists in forming a dry fabric reinforcement, by a punch and die process, before thermoset resin injection and consolidation [4]. The final properties of the obtained composite component are largely established during the shaping of the structure. In fact, this operation determines the fibre orientations and density, which influence directly the permeability of the preform, and thus the mechanical response of the composite part. Therefore, knowledge of the material behaviour and production parameters during such a process is important to determine the conditions for the successful manufacturing of a composite preform without macroscopic defects as wrinkles [5]. Defects also exist at lower scales. Their study needs additional mesoscopic and macroscopic analyses.

Different numerical models have been developed to study the shaping process of 2D composite reinforcements, using hypoelastic (see e.g. [6–8]) and hyperelastic (see e.g. [9,10]) constitutive equations. However, only few studies ([11,12]) have focused their attention on 3D woven fabrics. Their behaviour, due to the presence of through-thickness yarns is specific. Thus, a model capable to describe all the mechanisms involved during such a deformation process must be adopted. In [12] Charmetant et al. proposed a hyperelastic constitutive model for an initially orthotropic material, to simulate forming and three point bending of a 3D layer to layer angle interlock reinforcement.

In this work, the hyperelastic constitutive model detailed in [12] is adjusted to study the formability of a single layer E-glass non-crimp 3D orthogonal woven reinforcement (commercialized under trademark 3WEAVE® by 3Tex Inc.), on two complex shapes, i.e. tetrahedral and double-dome. The input data for the constitutive model are the experimental measurements of the in-plane shear, in-plane tension, transverse compression and transverse shear deformation response of the 3D reinforcement. The

* Corresponding author.
E-mail address: valter.carvelli@polimi.it (V. Carvelli).

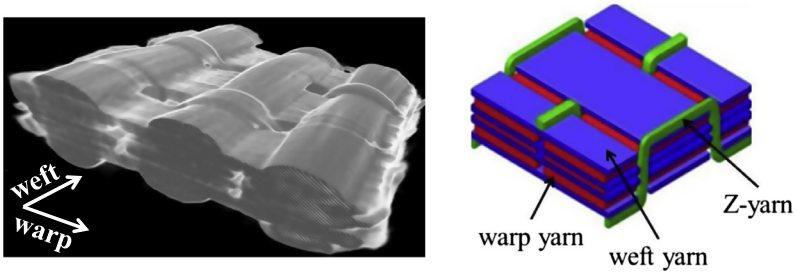

Fig. 1. Architecture of the yarns inside the non-crimp 3D orthogonal woven reinforcement: (a) μ-CT picture and (b) schematic of the unit cell. (For interpretation of the references to colour in this figure legend, the reader is referred to the web version of this article.)

Table 1
Features of the non-crimp 3D orthogonal woven reinforcement.

	Fabric plies	1
	Areal density (g/m^2)	3255
Warp	Insertion density (ends/cm)	2.76
	Top and bottom layer yarns (tex)	2275
	Middle layer yarns (tex)	1100
Weft	Insertion density (ends/cm)	2.64
	Yarns (tex)	1470
Z-yarns	Insertion density (ends/cm)	2.76
	Yarns (tex)	1800

experimental details and results for the considered 3D reinforcement are collected in [13,14].

The numerical results point out a good agreement with the experiments of such forming processes described in [15], and therefore, the capability of the constitutive model to predict the mechanical behaviour of the non-crimp 3D woven reinforcement during complex shaping.

2. Features of the non-crimp 3D orthogonal woven reinforcement

The textile is a single layer E-glass non-crimp 3D orthogonal woven reinforcement (3WEAVE® by 3Tex Inc.). The fibre architecture of the preform has three warp and four weft layers, interlaced by through-thickness (*Z*-directional) yarns (Fig. 1). The fabric construction results in ∼49%/∼49%/∼2% ratio of the fibre amounts (by volume) in the warp, weft and *Z* fibre directions, respectively. The same 3D woven reinforcement was used in the composite experimentally investigated in [16–18]. A detailed description of the 3D orthogonal weaving production process is presented in [19,20]. The fibre material is PPG Hybon 2022 E-glass. Some features of the non-crimp 3D orthogonal weave reinforcement are listed in Table 1. The reader is referred to [21] for observations of the reinforcement architecture in the composite.

3. Continuous hyperelastic model for large deformation analyses

The hyperelastic model adopted in this study is constructed on the hypothesis of an initially orthotropic material whose principal directions are: the warp direction $\overline{M}_1$, the weft direction $\overline{M}_2$ and a through-thickness direction $\overline{M}_3$. It also assumes that the contribution of each deformation mechanism is independent from the others (i.e. neglects the eventual coupling between different deformation modes). Therefore, the strain energy density function can be expressed as the summation of different strain energy density functions (each being a function of only one deformation mode).

The model considers as main deformation modes occurring during shaping and moulding processes of 3D textile composite reinforcements: (i) stretch in the warp direction; (ii) stretch in the weft direction; (iii) transverse compaction; (iv) in-plane shear; (v) transverse shear in the warp direction; and (vi) transverse shear in the weft direction.

For each deformation mode, a physical invariant and a strain energy density function based on the experimental behaviour of the reinforcement is defined (c.f. experimental results presented in [13,14]). The experimental behaviour is fitted analytically using an identification function based on a polynomial of the involved invariant. The experimental strain energy is used to determine the model parameters by means of a least squares algorithm, which minimizes the difference between the calculated and experimental energies (i.e. strain energy potential). The adopted strain energy density functions are presented in the following.

3.1. Stretch in warp and weft directions

The strain invariants (I_1^{elong} and I_2^{elong} in the warp and weft directions), which measure the Hencky deformations of the yarns, are calculated from the experimental results (see [13,14]). In Fig. 2 the tensile load-stretch invariant curves in warp and weft directions for the 3D woven fabric are depicted.

The strain energy density functions have been specifically chosen to describe the mechanical behaviour of the non-crimp 3D orthogonal weave reinforcement. The potential associated to stretch in warp direction (see Fig. 2a), is defined as:

$$\psi_1^{\text{elong}} = K_{L1}^{\text{elong}}(I_1^{\text{elong}})^2 + K_{L2}^{\text{elong}}(I_1^{\text{elong}})^3 + K_{L3}^{\text{elong}}(I_1^{\text{elong}})^4 + K_{L4}^{\text{elong}}(I_1^{\text{elong}})^5 \quad (1)$$

where K_{L1}^{elong}, K_{L2}^{elong}, K_{L3}^{elong}, K_{L4}^{elong} are parameters of the strain density function. The corresponding second Piola–Kirchhoff stress tensor is:

$$\overline{\overline{S}}_1^{\text{elong}} = \frac{1}{I_{41}}\overline{\overline{M}}_{11}\left[2K_{L1}^{\text{elong}}I_1^{\text{elong}} + 3K_{L2}^{\text{elong}}(I_1^{\text{elong}})^2 + 4K_{L3}^{\text{elong}}(I_1^{\text{elong}})^3 + 5K_{L4}^{\text{elong}}(I_1^{\text{elong}})^4\right] \quad (2)$$

At last, parameters K_{L1}^{elong}, K_{L2}^{elong}, K_{L3}^{elong}, K_{L4}^{elong} are identified following the mentioned identification procedure (see red line in Fig. 2). The structural tensors $\overline{M_{ij}}$ are constructed from the dyadic product between directions $\overline{M_i}$ and $\overline{M_j}$. The mixed invariants I_{4i} are built from the right Cauchy-Green tensor $\overline{\overline{C}}$ such that $I_{4i} = \overline{\overline{C}} : \overline{\overline{M}}_{ii}$. The complete description of the invariants as function of the strain tensor is detailed in.

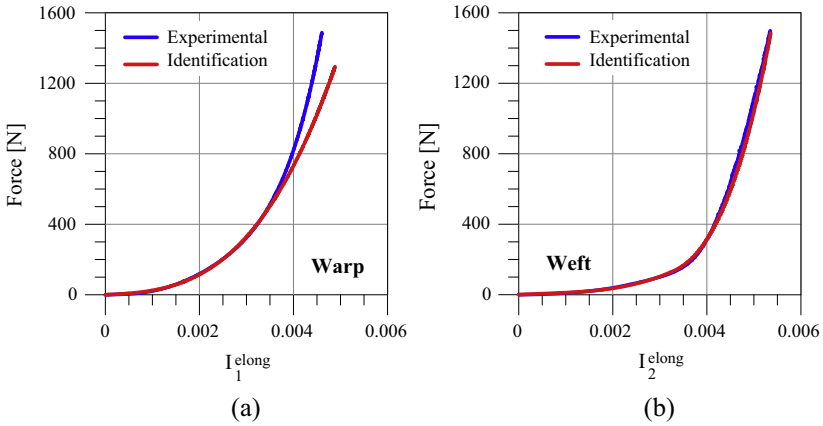

Fig. 2. Tension vs. stretch invariant $\left(I_1^{\text{elong}},\ I_2^{\text{elong}}\right)$ in: (a) warp and (b) weft direction for the non-crimp 3D woven reinforcement. (For interpretation of the references to colour in this figure legend, the reader is referred to the web version of this article.)

The fibre architecture of the preform (see Fig. 1) is different in warp and weft directions (see Fig. 2). Therefore, a strain energy density function for stretch deformation in weft direction (see Fig. 2b) is defined by:

$$\psi_2^{\text{elong}} = \begin{cases} K_{T1}^{\text{elong}}\left(I_2^{\text{elong}}\right)^2 + K_{T2}^{\text{elong}}\left(I_2^{\text{elong}}\right)^3 + K_{T3}^{\text{elong}}\left(I_2^{\text{elong}}\right)^4, & \text{if } I_2^{\text{elong}} \leqslant I_T^{\text{elong}} \\ K_{T4}^{\text{elong}} I_2^{\text{elong}} + K_{T5}^{\text{elong}}\left(I_2^{\text{elong}}\right)^2 + K_{T6}^{\text{elong}}\left(I_2^{\text{elong}}\right)^3 + K_{T7}^{\text{elong}}\left(I_2^{\text{elong}}\right)^4, & \text{else} \end{cases} \tag{3}$$

where I_T^{elong} is the invariant which determines the threshold between the initial and final behaviour. The associated second Piola–Kirchhoff stress tensor is:

$$\overline{\overline{S}}_2^{\text{elong}} = \frac{1}{I_{42}}\overline{\overline{M}}_{22} \begin{cases} 2K_{T1}^{\text{elong}} I_2^{\text{elong}} + 3K_{T2}^{\text{elong}}\left(I_2^{\text{elong}}\right)^2 + 4K_{T3}^{\text{elong}}\left(I_2^{\text{elong}}\right)^3, & \text{if } I_2^{\text{elong}} \leqslant I_T^{\text{elong}} \\ K_{T4}^{\text{elong}} + 2K_{T5}^{\text{elong}} I_2^{\text{elong}} + 3K_{T6}^{\text{elong}}\left(I_2^{\text{elong}}\right)^2 + 4K_{T7}^{\text{elong}}\left(I_2^{\text{elong}}\right)^3, & \text{else} \end{cases} \tag{4}$$

Currently, an experimental method to quantify longitudinal compression of woven fabrics (i.e. compression in the yarns direction) does not exist. Therefore, compression rigidity of the reinforcement is assumed to be 1% of the tensile one. This value makes compressive rigidity negligible without introducing numerical instabilities.

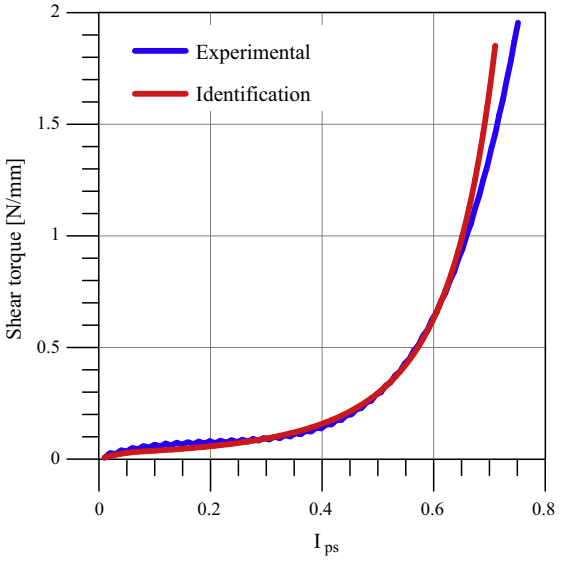

Fig. 3. Shear torque vs. strain invariant for the non-crimp 3D woven reinforcement. (For interpretation of the references to colour in this figure legend, the reader is referred to the web version of this article.)

3.2. In-plane shear

In the present hyperelastic constitutive model, the bias extension test (see details in [13]) is adopted to characterize the in-plane shear deformation mode. From the experimental results in Fig. 3 it is possible to distinguish two different behaviours. For small shear angles, the behaviour is nearly quadratic and becomes exponential for larger angles.

The in-plane shear invariant I_{ps} selected represents the sine of the shear angle. The threshold between both behaviours is given by invariant I_{ps}^0. Thus, the strain energy density function is defined:

$$\psi_{ps}(I_{ps}) = \begin{cases} \psi_{ps}^1(I_{ps}), & I_{ps} \leqslant I_{ps}^0 \\ \psi_{ps}^2(I_{ps}), & \text{else} \end{cases} \tag{5}$$

with

$$\psi_{ps}^1(I_{ps}) = K_{ps12} I_{ps}^2 + K_{ps13} I_{ps}^3,\ \psi_{ps}^2(I_{ps}) = K_{ps21}\left(1 - I_{ps}\right)^{-p_{22}} + \psi_{ps20}$$

and

$$K_{ps12} = \frac{K_{ps0}}{2}, K_{ps13} = \frac{K_{ps1} - K_{ps0}}{6I_{ps}^0}, K_{ps21} = \frac{K_{ps0} + K_{ps1}}{2p_{22}} I_{ps}^0 \left(1 - I_{ps}^0\right)^{1+p_{22}}$$

$$p_{22} = \frac{K_{ps1}\left(2 - 3I_{ps}^0\right) - K_{ps0} I_{ps}^0}{I_{ps}^0\left(K_{ps0} + K_{ps1}\right)}$$

$$\psi_{ps20} = \psi_{ps}^1(I_{ps}^0) - \psi_{ps}^2(I_{ps}^0) = K_{ps12}\left(I_{ps}^0\right)^2 + K_{ps13}\left(I_{ps}^0\right)^3 - K_{ps21}\left(1 - I_{ps}^0\right)^{-p_{22}} \tag{6}$$

The second Piola–Kirchhoff stress tensor is given by:

$$\overline{\overline{S}}_{\varphi}^{ps} = \left[\frac{1}{\sqrt{I_{41} I_{42}}}\left(\overline{\overline{M}}_{12} + \overline{\overline{M}}_{21}\right) - \frac{I_{ps}}{I_{41}}\overline{\overline{M}}_{11} - \frac{I_{ps}}{I_{42}}\overline{\overline{M}}_{22}\right] \times \begin{cases} 2K_{ps12} I_{ps} + 3K_{ps13}\left(I_{ps}\right)^2, & I_{ps} \leqslant I_{ps}^0 \\ p_{22} K_{ps21}\left(1 - I_{ps}\right)^{-p_{22}-1}, & \text{else} \end{cases} \tag{7}$$

Finally, parameters I_{ps}^0, K_{ps0}, K_{ps1} are determined by means of the mentioned procedure (see red line in Fig. 3). The identification procedure followed for in-plane shear deformation mode is based on the energy approach proposed by Harrison et al. in [22].

3.3. Transverse compaction

The transverse compaction deformation mode for the non-crimp 3D woven reinforcement is investigated by transverse

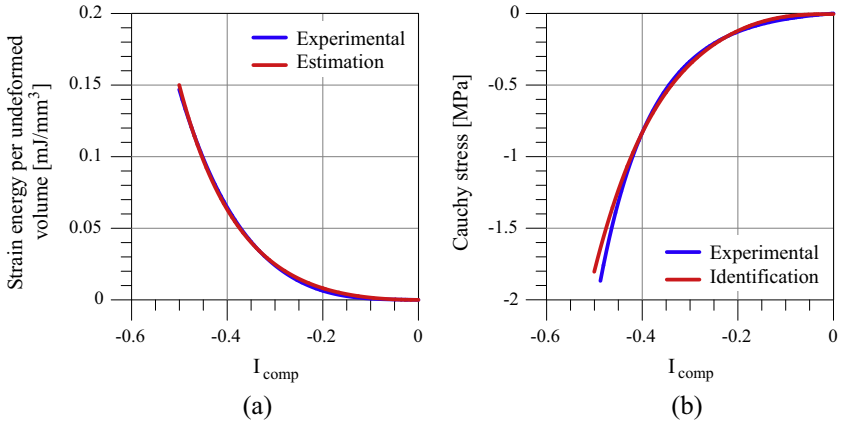

Fig. 4. Transverse compaction deformation mode: (a) strain energy per undeformed volume vs. stretch invariant and (b) cauchy stress vs. stretch invariant. (For interpretation of the references to colour in this figure legend, the reader is referred to the web version of this article.)

compression tests (see details in [14]). In Fig. 4 are depicted for the 3D fabric: strain energy per unit undeformed volume vs. transverse compaction invariant (Fig. 4a) and Cauchy stress vs. strain invariant (Fig. 4b). The transverse compaction invariant I_{comp} describes the Hencky strain of the thickness variation.

According to the behaviour observed in Fig. 4, the strain energy density function is assumed to be:

$$\psi_{\text{comp}} = K_{\text{comp}}\left[\left(1-\frac{I_{\text{comp}}}{I^0_{\text{comp}}}\right)^{-p} - p\frac{I_{\text{comp}}}{I^0_{\text{comp}}} - 1\right] \tag{8}$$

And, the corresponding second Piola–Kirchhoff stress tensor is:

$$\overline{\overline{S}}_{\text{comp}} = \frac{pK_{\text{comp}}}{I^0_{\text{comp}}}\left[1-\frac{I_{\text{comp}}}{I^0_{\text{comp}}}\right)^{-p-1} - 1\right]\left(\overline{\overline{C}}^{-1} - \frac{1}{I_{41}}\overline{\overline{M}}_1 - \frac{1}{I_{42}}\overline{\overline{M}}_2\right) \tag{9}$$

Parameters I^0_{comp}, p, K_{comp} are determined following the identification procedure above mentioned.

The material parameters identified in Sections 3.1–3.3 are listed in Table 2.

3.4. Transverse shear

Transverse shear plays a key role in bending deformation when the reinforcement is described as a 3D media. Numerical modelling of the bending behaviour of composite reinforcements during draping process is of first importance. The adopted transverse shear invariants I^{ts}_1 and I^{ts}_2 represents the sine of the shear angle in the warp and weft directions.

A purpose-built device has been developed in [12] in order to determine directly transverse shear properties of thick interlock reinforcements. The thickness of the reinforcement shown in Fig. 1 and analysed in the present paper is ≈2.54 mm, which is not enough for the transverse shear device to give meaningful results.

Alternatively, an inverse identification is performed on bending tests in order to determine the transverse shear properties. Cantilever bending response of specimens in warp and weft directions under own weight are numerically simulated and compared with the experimental results presented in [15]. The Levenberg–Marquardt algorithm is then used for the inverse identification [23]. The criterion adopted in this context was related to the bending performance, in particular to the curvature. Nevertheless, in order to reduce the complexity of the analysis, the total deflection at the tip of the specimen was selected as inspected value. This leads to assume that if the deflection of the numerical simulation is close to the experimental data, the curvature is also comparable. Initial calculations are performed assuming the transverse shear rigidity equal to the in-plane one, as tentative value, and an initial error is calculated, using the least squares method. Identification of one parameter, for each transverse plane (φ = 1, 2), is thus performed by the optimization. The strain energy density function is assumed to be in the form:

$$\psi^{ts}_{\varphi}(I^{ts}_{\varphi}) = K^{ts\varphi}_1 (I^{ts}_{\varphi})^2 \quad \varphi = 1,2 \tag{10}$$

Specimens are discretized with hexahedral elements of size 2 mm × 2 mm × 0.5 mm. Four elements are used in the thickness (see Fig. 5a) in order to display a proper deflection.

Comparisons in terms of maximum tip's deflection between experimental and numerical simulations of bending tests are listed in Table 3. The use of only one parameter for each direction leads to higher differences for some lengths. Additional parameters would improve the numerical behaviour but would increase the inverse identification complexity. Finally, the transverse shear parameters as input in the hyperelastic model, adopted for the simulation of the formability of the non-crimp 3D woven reinforcement, are listed in Table 4.

Three dimensional finite elements with displacement degrees of freedom do not have directly identifiable bending rigidities. Bending of thick fabrics is governed by the transverse shear and tensile rigidities. When the current material is submitted to in-

Table 2
Identified parameters for the hyperelastic constitutive model of the non-crimp 3D weave E-glass composite reinforcement.

Stretch in warp direction (MPa)		Transverse compaction	
K^{elong}_{L1}	50.14	I^0_{comp}	−1.675
K^{elong}_{L2}	7494.69	p	8.613
K^{elong}_{L3}	19816948.88	K_{comp}	0.008
K^{elong}_{L4}	129459569.30		
Stretch in weft direction (MPa)		**In-plane shear**	
K^{elong}_{T1}	60.18	I^0_{ps}	0.076
K^{elong}_{T2}	−22312.10	K_{ps0}	0.371
K^{elong}_{T3}	10056816.47	K_{ps1}	0.068
K^{elong}_{T4}	−3.40		
K^{elong}_{T5}	3151.09		
K^{elong}_{T6}	−958953.86		
K^{elong}_{T7}	104667095.12		
I^{elong}_{T}	0.003		

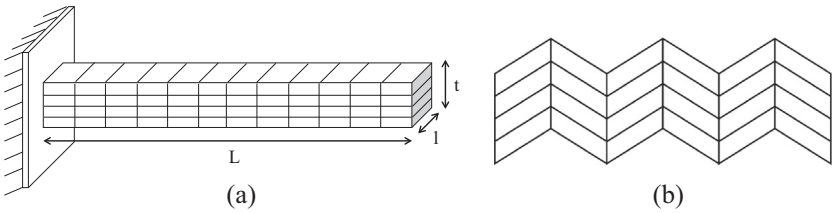

Fig. 5. (a) Mesh for cantilever bending test numerical simulations and (b) non-physical wrinkling with compression stiffness.

Table 3
Tip deflection in the warp and weft directions for transverse shear parameters identification.

Warp	Specimen length L (mm)	200	250	300	350			
	Experimental tip deflection (mm)	52.71	163.15	245.72	281.17			
	Numerical tip deflection (mm)	79.9	153.4	224.5	289.4			
	Difference to experimental data (%)	+51.6	−6.4	−8.6	+2.9			
Weft	Specimen length L (mm)	200	250	300	350	400	450	500
	Experimental tip deflection (mm)	5.47	13.54	29.78	49.98	103.20	184.26	296.87
	Numerical tip deflection (mm)	5.5	15.1	31.6	59.3	98.1	151.7	214.4
	Difference to experimental data (%)	0	+11.9	+6.0	+18.6	−4.9	−17.7	−27.8

Table 4
Transverse shear parameters for the hyperelastic model of the non-crimp 3D weave E-glass composite reinforcement.

Transverse shear in warp direction (MPa)		Transverse shear in weft direction (MPa)	
K_1^{ts1}	0.7345	K_1^{ts2}	43.207

plane compression, non-physical wrinkling (see Fig. 5b), which lead to local bending, appears easily thanks to the extremely low transverse shear rigidities. The sharp angles in Fig. 5b between elements are obviously not observed experimentally. In order to prevent this phenomenon, a method to introduce a bending rigidity linked to the change in curvature should be implemented as in [12]. Such a feature inside three dimensional elements imply the use of a more complex continuum theory, as the second gradient one [24], which is not available in commercial codes.

In the current case, the choice of the in-plane compression stiffness was as mentioned in Section 3.1. The compression parameters are taken as one percent of the initial tensile rigidities in each direction.

4. Finite element simulations and comparison with experiments

Finite element simulations of the non-crimp 3D orthogonal weave E-glass composite reinforcement forming are performed using Abaqus/Explicit finite element code [25]. The explicit analyses have been demonstrated to be suitable for non-linear geometric and material problems, in particular where a large number of contacts between the parts occur ([26,27]). The hyperelastic constitutive model for an initial orthotropic material is implemented through a user material subroutine VUMAT within Abaqus/Explicit.

The validity of the continuous hyperelastic constitutive model is first assessed by comparing experimental and numerical main deformation modes (e.g. in-plane shear) and then the forming of the non-crimp 3D orthogonal woven reinforcement.

Table 5
Parameters for numerical simulations of bias extension test.

Type of analysis	Dynamic, explicit
Imposed displacement (mm)	40
Time period (s)	100
Mesh size 11.78 mm	
Element type	C3D8
Total number of elements	162
Total number of nodes	398
Mesh size 3.53 mm	
Element type	C3D8
Total number of elements	1660
Total number of nodes	3562

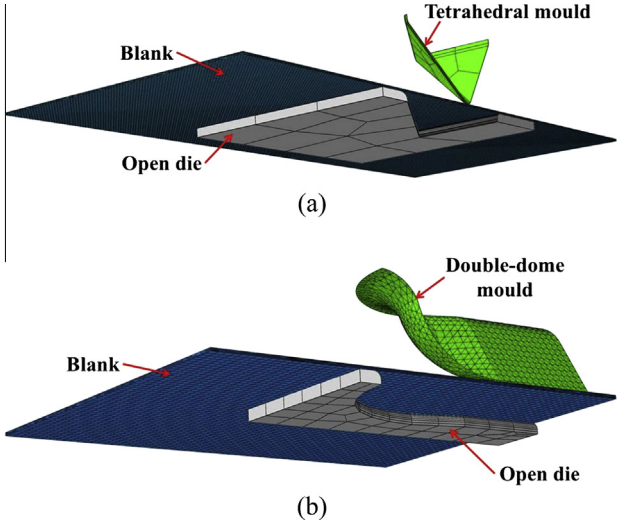

Fig. 6. Finite element model for: (a) tetrahedron and (b) double-dome forming tests. (For interpretation of the references to colour in this figure legend, the reader is referred to the web version of this article.)

4.1. Features of the finite element modelling of bias extension test

Bias extension tests involve rectangular specimen of material such that the warp and weft directions of the tows are orientated initially at ±45° to the direction of the applied tension load. Bias tests, as well as picture frame tests, are adopted to characterize the in-plane shear behaviour of textile reinforcements for composites.

Three regions with different shear angles develop during bias extension test of a woven fabric [28]. At the macroscopic scale, the shear angle is discontinuous at the borders of these shear regions. These discontinuities cannot be modelled within the stan-dard finite elements, which exhibit tension locking (also called intra-ply shear locking, i.e. the inability of standard finite elements to represent accurately the in-plane shear deformation in fibre reinforced materials). This results in unrealistically high fibre stresses in non-aligned elements and makes the elements overly stiff [29].

In order to overcome this problem, the simplest way is to align the element edges with the direction of the fibres ([29–31]) (see Fig. 8a and b). When the element edges coincide with the lines of discontinuity in the shear field, the discontinuities in the shear angle can be represented correctly and no locking is present in the simulation.

In the current case, as shown in Fig. 8a and b, the element edges are oriented with warp and weft (i.e. at ±45° with respect to the

Table 6
Parameters for tetrahedron and double-dome forming simulations.

	Parameter	Tetrahedron	Double-dome 0°/90°	Double-dome ±45°
	Type of analysis	Dynamic, explicit	Dynamic, explicit	Dynamic, explicit
	Punch displacement (mm)	65	65	65
	Time period (s)	400	400	400
	Mass scaling factor	10	30	30
	Material density (kg/m^3)	1.596 E−4	1.596 E−4	1.596 E−4
Fabric to tools interaction	Type of contact	Surface-to-surface	Surface-to-surface	Surface-to-surface
	Tangential behaviour	Friction (coefficient 0.2)	Friction (coefficient 0.2)	Friction (coefficient 0.2)
	Normal behaviour	Exponential	Exponential	Exponential
Mould	Type	3D rigid body	3D rigid body	3D rigid body
	Element type	R3D4	R3D3	R3D3
	Total number of elements	105	496	496
	Total number of nodes	120	278	278
Open die	Type	3D rigid body	3D rigid body	3D rigid body
	Element type	R3D4	R3D4	R3D4
	Total number of elements	116	816	816
	Total number of nodes	99	831	831
Blank 1	Mesh size (mm)	5	5	4.24
	Element type	C3D8	C3D8	C3D8
	Total number of elements	24,000	14,400	20,400
	Total number of nodes	30,855	18,605	26,505
	Elements through thickness	4	4	4
Blank 2	Mesh size (mm)	3	3	2.12
	Element type	C3D8	C3D8	C3D8
	Total number of elements	66,400	40,000	80,800
	Total number of nodes	84,420	51,005	103,005
	Elements through thickness	4	4	4

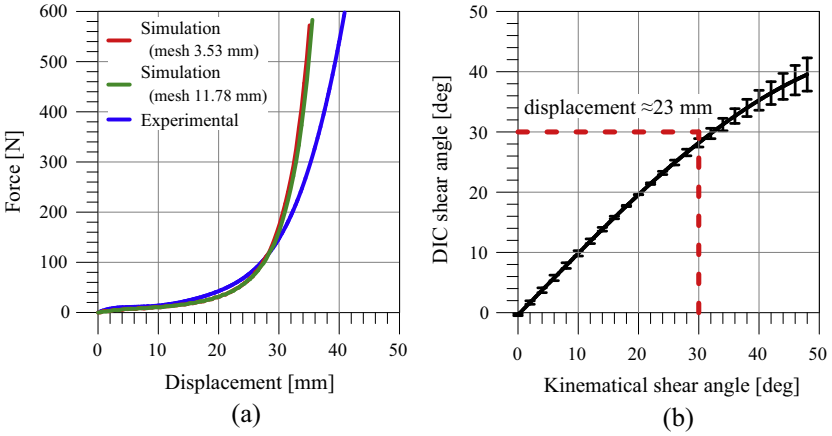

Fig. 7. (a) Force–displacement curves for bias tension tests. Comparison between numerical simulations and experimental results. (b) Measured and kinematical shear angle for bias extension tests. Average curve with standard deviation (error bars) of five tests (from [13]). (For interpretation of the references to colour in this figure legend, the reader is referred to the web version of this article.)

sides of the specimen). In addition, two distinct element sizes are utilized to assess the sensitivity of this parameter on the numerical results. The specimen's geometry and testing conditions detailed in [13] were adopted in the finite element analyses. Some details of the numerical models are reported in Table 5.

4.2. Features of the finite element modelling of forming processes

The tetrahedral and double-dome shape forming processes detailed in [15], are numerically simulated. The tools geometry, blank dimensions and test parameters used for finite element

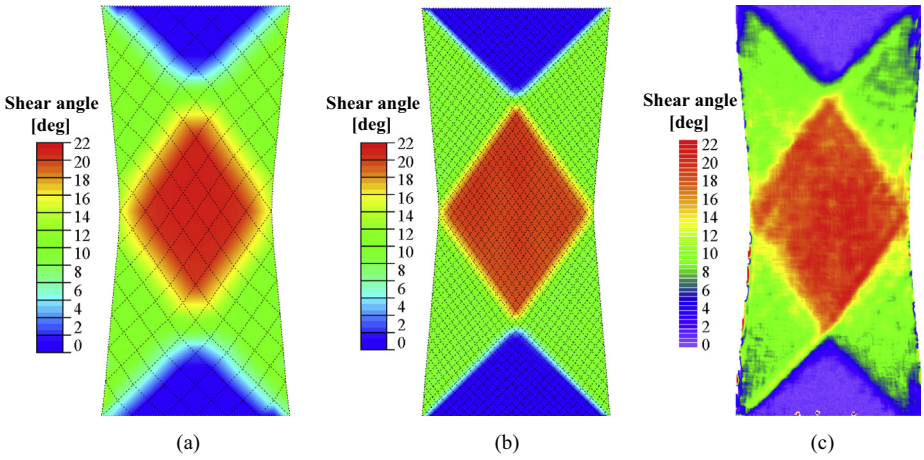

Fig. 8. Comparison between numerical and experimental shear angle distribution during bias extension test for a theoretical shear angle of ≈22°. Finite element simulations for a mesh size of (a) 11.78 and (b) 3.53 mm. (c) Shear angle distribution on the reinforcement surface measured by DIC. (For interpretation of the references to colour in this figure legend, the reader is referred to the web version of this article.)

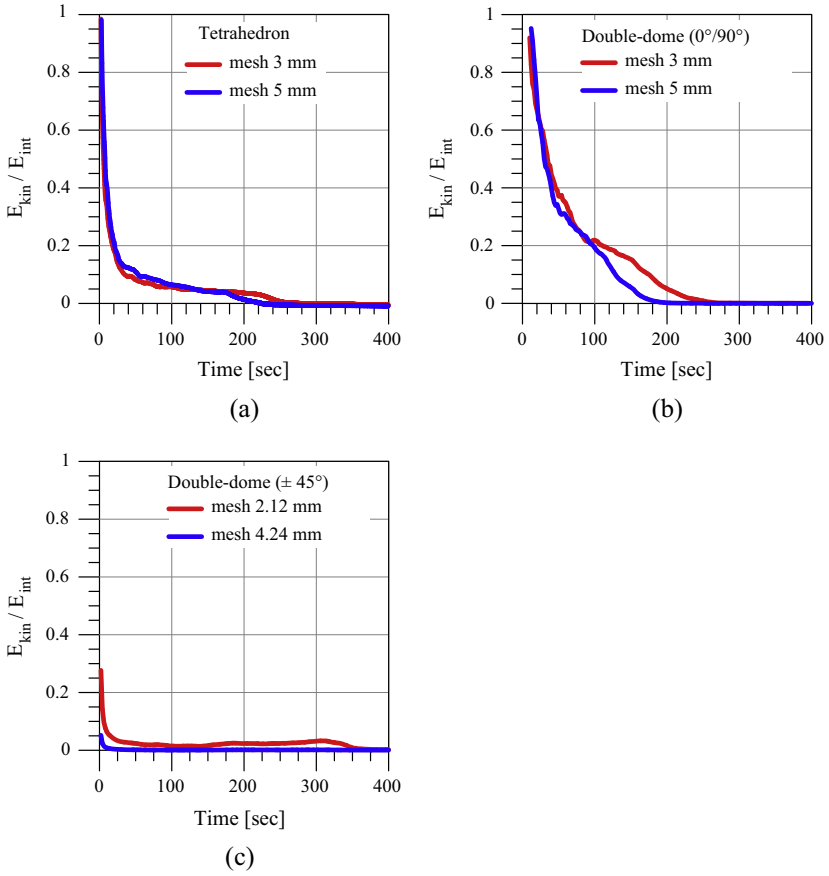

Fig. 9. Ratio of kinetic (E_{kin}) to internal energy (E_{int}) of the blank during: (a) tetrahedron; double-dome forming simulations for yarn orientations of: (b) 0°/90° and (c) ±45°. (For interpretation of the references to colour in this figure legend, the reader is referred to the web version of this article.)

modelling are the same adopted in the experiments (see details in [15]). As shown in Fig. 6, due to the symmetries of the moulds, only half and quarter of the experimental set-up are considered for tetrahedron and double-dome numerical models, respectively. Blanks are discretized with hexahedral elements, while steel open dies and punches are treated as rigid bodies using four-node rigid elements. Moreover, due to the importance of out-of-plane properties of the 3D reinforcement, the specimen thickness is discretized with four elements. The parameters for tetrahedron and double-dome shaping simulations are listed in Table 6.

Tetrahedron forming simulations are performed for two different mesh sizes (i.e. 3 and 5 mm), to evaluate the effect of this parameter on the results. Numerical analyses are carried out on blanks having the initial direction of the warp and weft parallel to the sides of the die (see Fig. 6a).

Double-dome shaping simulations are carried out on blanks having the initial direction of the warp and weft parallel to the sides of the die (orientations named 0°/90°, Fig. 6b), and with yarns at ±45° with respect to the sides of the open die (orientations named ±45°). Two different element sizes are adopted for blanks initially oriented at 0°/90° (mesh size of 3 and 5 mm) and ±45°(mesh size of 2.12 and 4.24 mm). In the case of yarns orientation of ±45°, the element edges are oriented with warp and weft direc-tions, to overcome the numerical artefact of intra-ply shear locking.

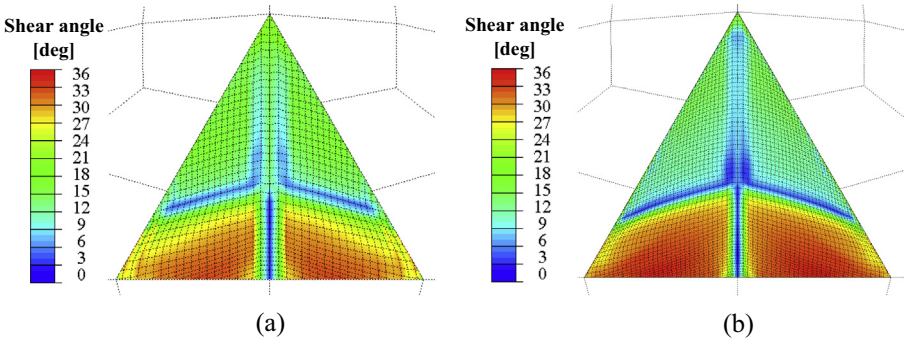

Fig. 10. Shear angle distribution at the end of tetrahedral mould shaping for numerical simulations with mesh size of: (a) 5 and (b) 3 mm. (For interpretation of the references to colour in this figure legend, the reader is referred to the web version of this article.)

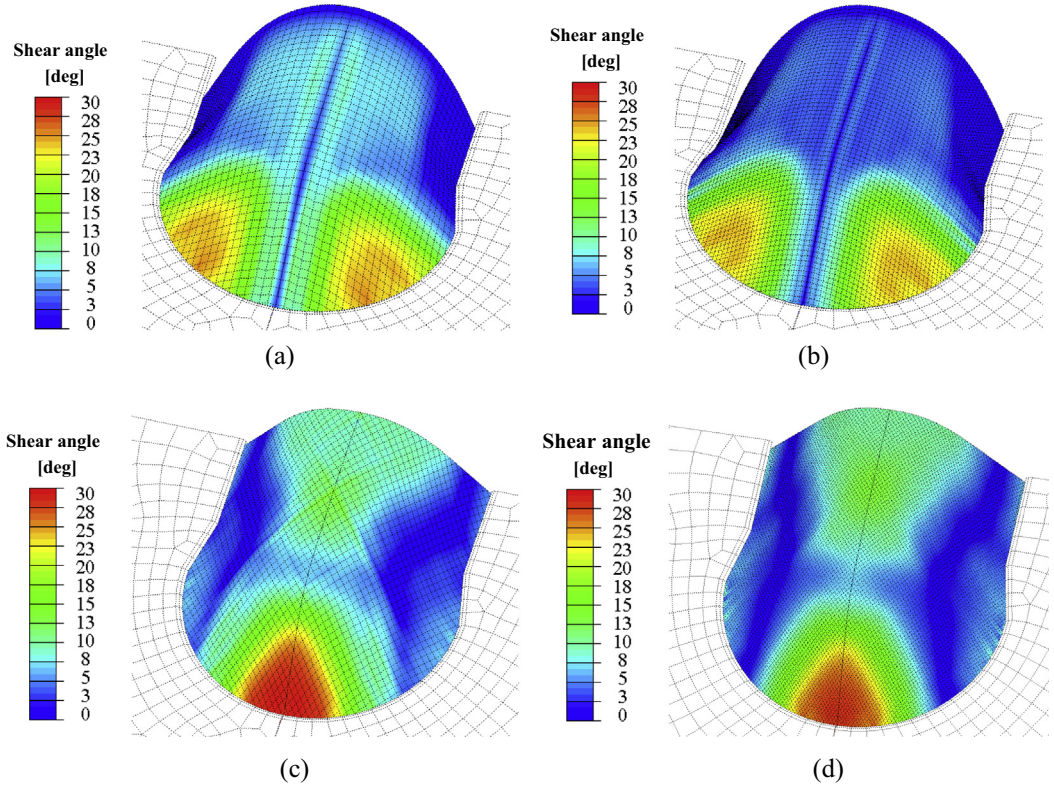

Fig. 11. Map of shear angles at conclusion of double-dome draping. Finite element simulations for: blank oriented at 0°/90°, mesh size (a) 5 and (b) 3 mm; blank oriented at ±45°, mesh size (c) 4.24 and (d) 2.12 mm. (For interpretation of the references to colour in this figure legend, the reader is referred to the web version of this article.)

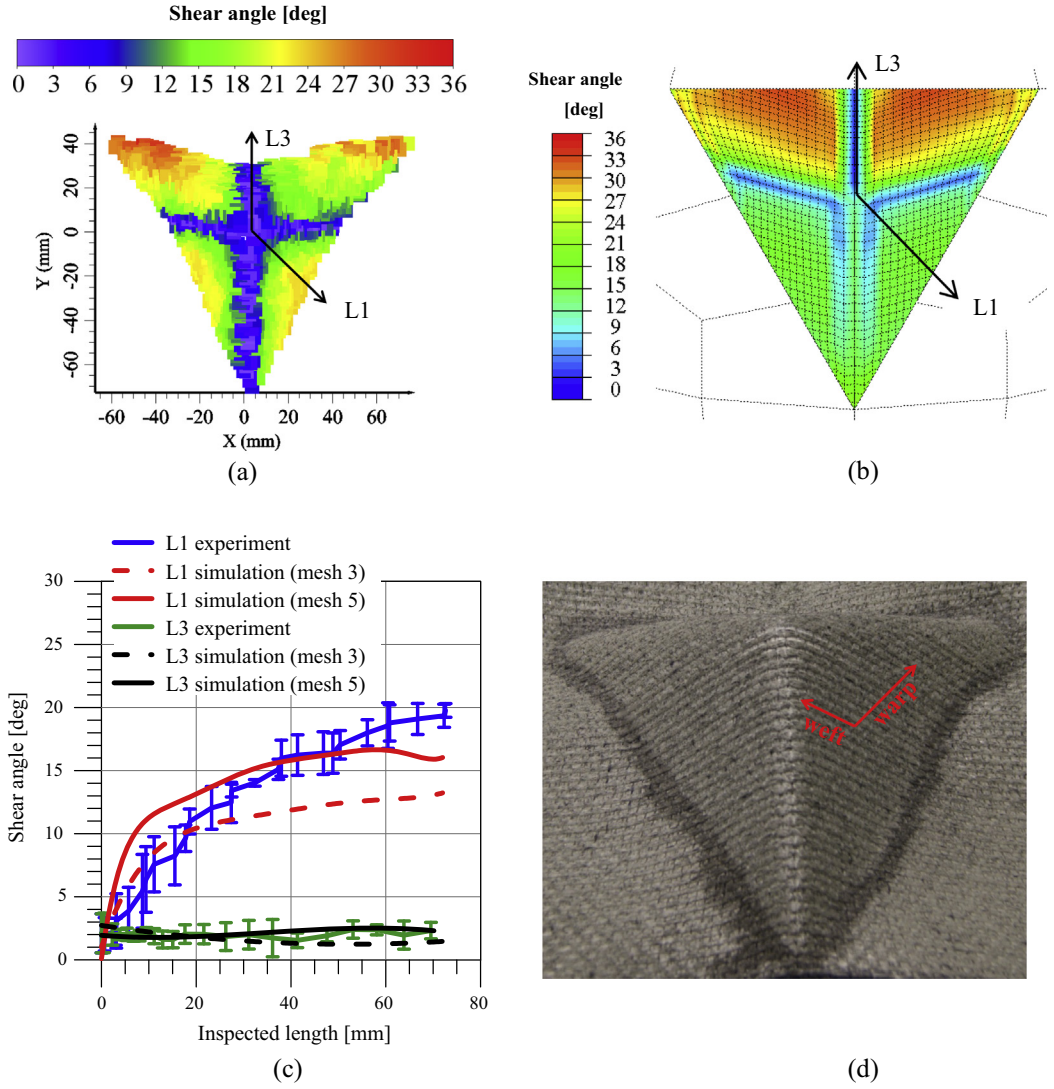

Fig. 12. Tetrahedral shape forming test. Shear angle distribution at the end of draping process: (a) experimental; (b) numerical simulation for a mesh size of 5 mm; (c) along paths *L*1 and *L*3 (error bars give the standard deviation of four tests). (d) Experimental deformed shape of the 3D woven reinforcement at the end of the forming. (For interpretation of the references to colour in this figure legend, the reader is referred to the web version of this article.)

4.3. Validation of finite element simulations with experiments

4.3.1. Bias extension test

Fig. 7a presents the comparison between experiments and finite element simulations of bias extension test for the 3D woven reinforcement. The force vs. displacement curves show a good agreement between experimental and numerical results up to an imposed displacement of ≈30 mm, corresponding to a kinematical shear angle of about 44°. As detailed in [13], measured and kinematical shear angles are in good agreement up to ≈30° (see Fig. 7b). In fact, for a theoretical shear angle of ≈22° (see Fig. 8c) the shear angle distribution on the specimen surface, measured by means of digital image correlation ([13]), is the one assumed by the theoretical model [22].

Moreover, the comparison illustrated in Fig. 7a demonstrates a good agreement between finite element simulations with two different mesh sizes. From the results in Fig. 8a and b, it can be noticed that decreasing the mesh size, the capability of the numer-ical model to describe the experimental shear angle distribution increases. Nevertheless, the mesh size does not affect the accuracy of the results in terms of force and displacements (see Fig. 7a).

4.3.2. Tetrahedron and double-dome forming simulations

The quasi-static response in the numerical analysis using an explicit numerical code is demonstrated with a negligible inertia effect. This requirement is satisfied when the kinetic energy (E_{kin}) of the blank is lower than 5% of the internal energy (E_{int}), after a certain time of the deformation process ([32]).

Fig. 9 depicts the ratio of kinetic (E_{kin}) to internal energy (E_{int}) of the blank, during tetrahedral and double-dome shape forming process simulations. The curves in Fig. 9a–c, for all the element sizes adopted, show that the kinetic to internal energy ratio of the blank is smaller than 5% of the strain energy. This means that the finite element simulations are not affected by dynamic effects.

Since the shear deformation is the primary deformation mechanism during shaping, Figs. 10 and 11, illustrate the map of shear angle on the blank at the end of tetrahedron and double-dome draping processes. The plots demonstrate a negligible influence of the mesh size on the shear angle distribution.

The experimental investigation detailed in [15] provides measurements of the shear angle distribution during the forming processes with the two moulds by 3D DIC. The comparison of the finite

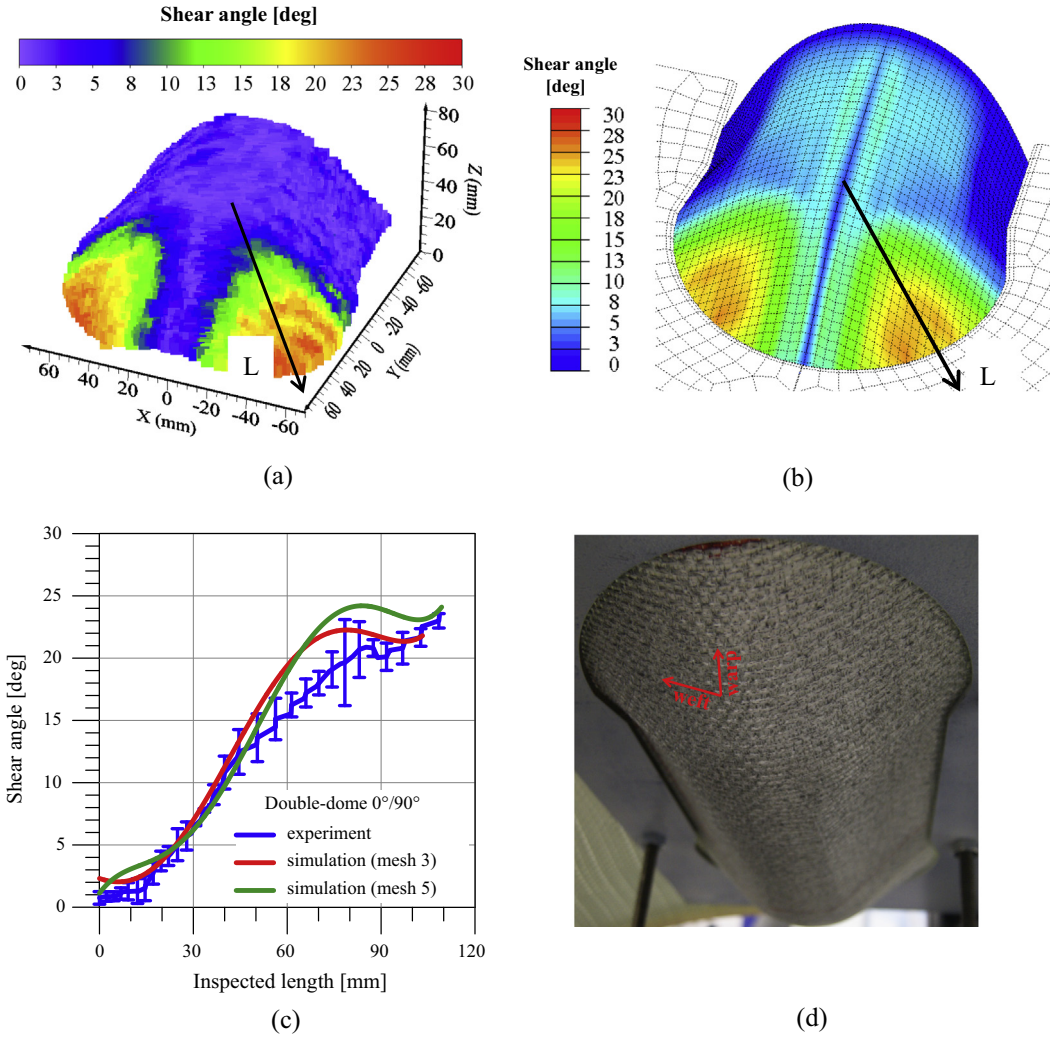

Fig. 13. Double-dome forming tests for fabric with yarn orientations 0°/90°. Shear angle distribution at the end of draping process: (a) experimental; (b) numerical simulation for a mesh size of 5 mm; (c) along path *L* (error bars give the standard deviation of four tests). (d) Experimental deformed shape of the 3D woven reinforcement at the end of the forming. (For interpretation of the references to colour in this figure legend, the reader is referred to the web version of this article.)

element and experimental shear angle distribution are detailed in Figs. 12a and b, 13a and b, and 14a and b, at the end of tetrahedron and double-dome forming (i.e. mould displacement of ≈65 mm). The contour maps demonstrate global agreement between experimental and numerical shear angles distribution on the entire external surface of the 3D fabric. Moreover, shear angles are detailed along some selected paths (lines *L*1, *L*3 in Fig. 12a and line L in Figs. 13a and 14a).

The numerical predictions in Fig. 12c show similar results to the experimental value of the local shear angle along both paths at conclusion of tetrahedral shape forming, mainly with the coarse mesh. Judging the graphs in Fig. 13c, experimental and numerical analyses provide analogous shear angles distributions for specimens initially oriented at 0°/90°. While, for blanks initially oriented at ±45° (see Fig. 14c), finite element simulations provide quite a bit higher shear angles than those experimentally observed.

The agreement of the above mention experimental and numerical distributions of the shear angle, as well as the global shape without wrinkles (as observed in the experiments Figs. 12d, 13d and 14d), points out the capability of the adopted hyperelastic model to describe the correct deformation behaviour of the non-crimp 3D orthogonal weave textile. Nevertheless the numerical and experimental onset and development of wrinkles should be compared on other tests and other reinforcements.

5. Conclusions

In this work, a hyperelastic model is implemented to study the formability of a single layer E-glass non-crimp 3D orthogonal woven reinforcement (commercialized under trademark 3WEAVE® by 3Tex Inc.) into tetrahedral and double-dome shapes.

The input data for the material model are obtained by the experimental response of the 3D fabric under different deformation modes, presented in previous publications.

The adopted hyperelastic model takes into consideration the contribution of in-plane and out-of-plane deformation mechanisms as independent each other: stretch in warp and weft direction; in-plane shear; transverse compaction; and transverse shear in warp and weft direction. The model was first assessed comparing the experiments and finite element simulations of bias extension test for the 3D woven reinforcement, being the in-plane shear one of the most important deformation modes. The good agreement was observed with different mesh sizes in predicting

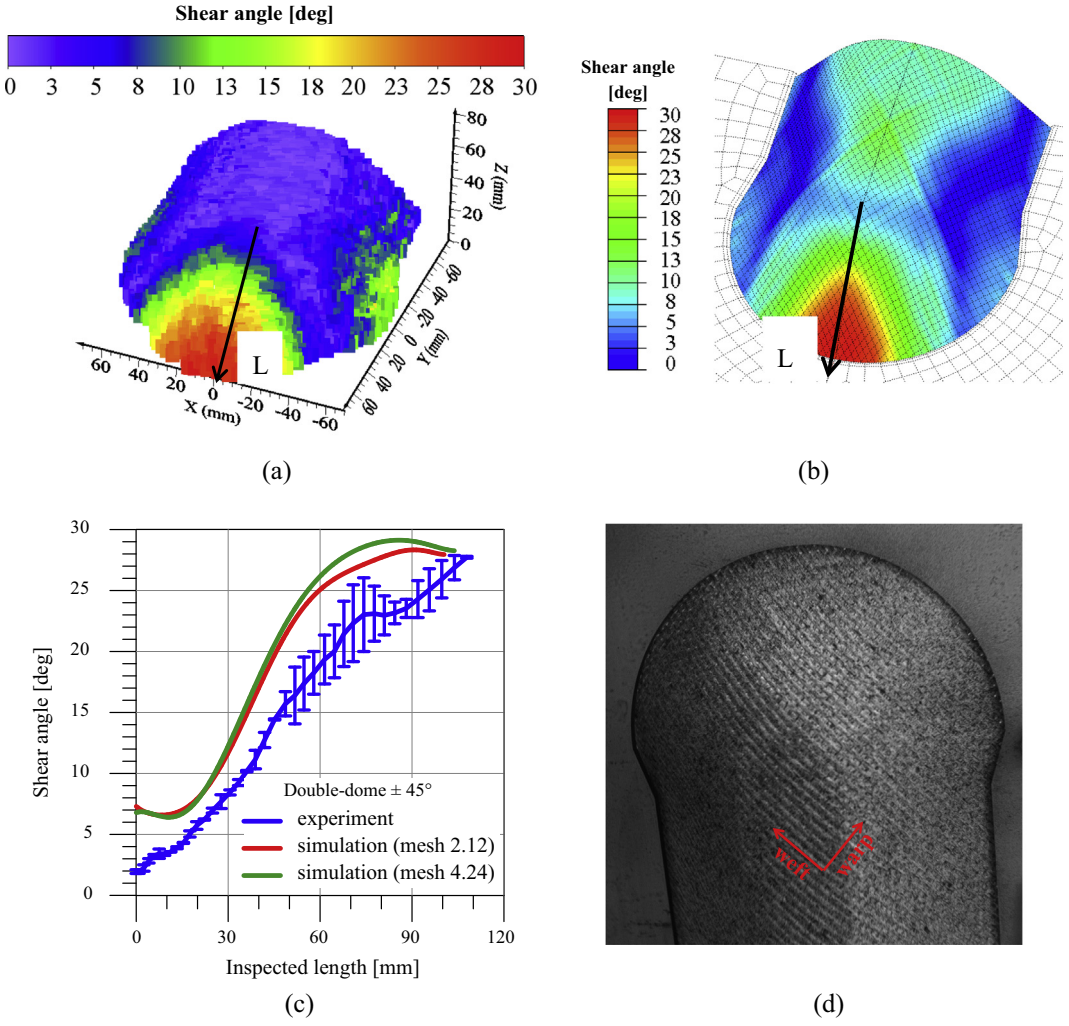

Fig. 14. Double-dome forming tests for blank with yarn orientations ± 45°. Shear angle distribution at the end of draping process: (a) experimental; (b) finite element modelling for a mesh size of 4.24 mm; (c) along path *L* (error bars give the standard deviation of four tests). (d) Experimental deformed shape of the 3D woven reinforcement at the end of the forming. (For interpretation of the references to colour in this figure legend, the reader is referred to the web version of this article.)

the global response up to about 44° and the shear angle distribution.

Finally, the numerical simulations were focused on forming of a tetrahedral and a double-dome shape, using an explicit numerical code, showing: the negligible influence of the mesh size; the global good agreement between experimental and numerical shear angles distribution on the entire external surface of the blanks; the similar to the experimental local shear angle along some paths at conclusion of the forming.

Finite element simulations and experimental results demonstrated the adequacy of the adopted hyperelastic model to describe the deformation mechanisms involved during draping and the efficiency to predict the global behaviour of the non-crimp 3D woven reinforcement during complex shape forming.

The hyperelastic model presented in this study provides an efficient numerical tool useful for the optimization of the forming process of any complex shape with such 3D reinforcement.

Acknowledgements

3Tex Inc. is acknowledged for manufacturing and supplying the non-crimp 3D orthogonal weave E-glass reinforcement (3WEAVE®). The research visit of J. Pazmino to INSA Lyon and K.U. Leuven was partially supported by Laboratoire de Mécanique des Contacts et des Solides and INFUCOMP (FP7) project, respectively.

References

[1] Mouritz AP. Three-dimensional (3D) fibre reinforcements for composites. In: Boisse Philippe, editor. Composite reinforcements for optimum performance. UK: Woodhead Publishing; 2011. p. 157–99.
[2] Stig F, Hallström S. A modelling framework for composites containing 3D reinforcement. Compos Struct 2012;94:2895–901.
[3] Advani SG, Sozer ME. Process modeling in composites manufacturing. Marcel Dekker; 2003.
[4] de Bilbao E, Soulat D, Hivet G, Gasser A. Experimental study of bending behaviour of reinforcements. Exp Mech 2010;50:333–51.
[5] Allaoui S, Boisse P, Chatel S, Hamila N, Hivet G, Soulat D, et al. Experimental and numerical analyses of textile reinforcement forming of a tetrahedral shape. Composites: Part A 2011;42:612–22.
[6] Peng XQ, Cao J. A continuum mechanics-based non-orthogonal constitutive model for woven composite fabrics. Compos Sci Technol 2005;36:859–74.
[7] Khan MA, Mabrouki T, Vidal-Sallè E, Boisse P. Numerical and experimental analyses of woven composite reinforcement forming using a hypoelastic behaviour. Application to the double dome benchmark. J Mater Process Technol 2010;210:378–88.
[8] Yu WR, Harrison P, Long A. Finite element forming simulation for non-crimp fabrics using a non-orthogonal constitutive equation. Composites: Part A 2005;36:1079–93.
[9] Aimène Y, Vidal-Sallé E, Hagège B, Sidoroff F, Boisse P. A hyperelastic approach for composite reinforcement large deformation analysis. J Compos Mater 2010;44(1):5–26.

[10] Charmetant A, Vidal-Sallé E, Boisse P. Hyperelastic modelling for mesoscopic analyses of composite reinforcements. Compos Sci Technol 2011;71:1623–31.
[11] De Luycker E, Morestin F, Boisse P, Marsal D. Simulation of 3D interlock composite preforming. Compos Struct 2009;88:615–23.
[12] Charmetant A, Orliac JG, Vidal-Sallè E, Boisse P. Hyperelastic model for large deformation analyses of 3D interlock composite preforms. Compos Sci Technol 2012;72:1352–60.
[13] Carvelli V, Pazmino J, Lomov SV, Verpoest I. Deformability of a non-crimp 3D orthogonal weave E-glass composite reinforcement. Compos Sci Technol 2012;73:9–18.
[14] Pazmino J, Carvelli V, Lomov SV. Micro-CT analysis of the internal deformed geometry of a non-crimp 3D orthogonal weave E-glass composite reinforcement. Composites Part B 2014;65:147–57.
[15] Pazmino J, Carvelli V, Lomov SV. Formability of a non-crimp 3D orthogonal weave E-glass composite reinforcement. Compos Part A: Appl Sci Manuf 2014;61:76–83.
[16] Carvelli V, Gramellini G, Lomov SV, Bogdanovich AE, Mungalov DD, Verpoest I. Fatigue behaviour of non-crimp 3D orthogonal weave and multi-layer plain weave E-glass reinforced composites. Compos Sci Technol 2010;70:2068–76.
[17] Lomov SV, Bogdanovich AE, Ivanov DS, Karahan M, Verpoest I. A comparative study of tensile properties of non-crimp 3D orthogonal weave and multilayer plain weave E-glass composites. Part1: materials, methods and principal results. Composites: Part A 2009;40:1134–43.
[18] Ivanov DS, Lomov SV, Bogdanovich AE, Karahan M, Verpoest I. A comparative study of tensile properties of non-crimp 3D orthogonal weave and multi-layer plain weave E-glass composites. Part 2: comprehensive experimental results. Composites Part A 2009;40:1144–52.
[19] Mohamed MH, Zhang ZH. Method of forming variable cross-sectional shaped three-dimensional fabrics. US Patent 5085252, 4 February 1992.
[20] Bogdanovich AE. Advancements in manufacturing and applications of 3D woven preforms and composites. In: Proceeding of 16th international conference on composite materials (ICCM 16), Kyoto-Japan; 2007.
[21] Desplentere F, Lomov SV, Woerdeman DL, Verpoest I, Wevers M, Bogdanovich A. Micro-CT characterization of variability in 3D textile architecture. Compos Sci Technol 2005;65:1920–30.
[22] Harrison P, Clifford MJ, Long AC. Shear characterization of viscous woven textile composites: a comparison between picture frame and bias extension experiments. Compos Sci Technol 2004;64:1454–65.
[23] Schnur DS, Zabaras N. An inverse method for determining elastic material properties and a material interface. Int J Numer Methods Eng 1992;33:2039–57.
[24] Ferretti M, Madeo A, dell'Isola F, Boisse P. Modeling the onset of shear boundary layers in fibrous composite reinforcements by second-gradient theory. Zeitschrift für angewandte Mathematik und Physik 2014;65:587–612.
[25] Dassault Systemes – Abaqus/Explicit <http://www.3ds.com/products-services/simulia/portfolio/abaqus/abaqus-portfolio/abaqusexplicit/>.
[26] Belytschko T, Liu W, Moran B, Elkhodary K. Nonlinear finite elements for continua and structures. John Wiley & Sons; 2013.
[27] Vanclooster K, Lomov SV, Verpoest I. Experimental validation of forming simulations of fabric reinforced polymers using an unsymmetrical mould configuration. Composites: Part A 2009;40:530–9.
[28] Lebrun G, Bureau MN, Denault J. Evaluation of bias-extension and picture frame test methods for the measurement of intraply shear properties of PP/glass commingled fabrics. Compos Struct 2003;61:341–52.
[29] Ten Thije RHW, Akkerman R. Solutions to intra-ply shear locking in finite element analyses of fibre reinforced materials. Compos Part A: Appl Sci Manuf 2008;39:1167–76.
[30] Hamila N, Boisse P. Locking in simulation of composite reinforcement deformations. Analysis and treatment. Composites: Part A 2013;53:109–17.
[31] Yu B, Cartwright B, McGuckin D, Ye L, Mai Y-W. Intra-ply shear locking in finite element analyses of woven fabric forming processes. Compos Part A: Appl Sci Manuf 2006;37:790–803.
[32] Sun JS, Lee KH, Lee HP. Comparison of implicit and explicit finite element methods for dynamic problems. J Mater Process Technol 2000;105:110–8.